Nano Research
2021, 14(12): 4857–4864
ISSN 1998-0124 CN 11-5974/O4
https://doi.org/10.1007/s12274-021-3445-5

Research Article

Multi-interface collaboration of graphene cross-linked NiS-NiS_2-Ni_3S_4 polymorph foam towards robust hydrogen evolution in alkaline electrolyte

Haiqing Wang[1,§] (✉), Wenjing Zhang[2,§], Xiaowei Zhang[1], Shuxian Hu[2] (✉), Zhicheng Zhang[3], Weijia Zhou[1], and Hong Liu[1,4] (✉)

[1] *Collaborative Innovation Center of Technology and Equipment for Biological Diagnosis and Therapy in Universities of Shandong, Institute for Advanced Interdisciplinary Research (iAIR), University of Jinan, Jinan 250022, China*
[2] *Beijing Computational Science Research Center, Beijing 100193, China*
[3] *Tianjin Key Laboratory of Molecular Optoelectronic Sciences, Department of Chemistry, School of Science, Tianjin University, Tianjin 300072, China*
[4] *State Key Laboratory of Crystal Materials, Shandong University, Jinan 250100, China*
[§] *Haiqing Wang and Wenjing Zhang contributed equally to this work.*

Received: 24 February 2021 / **Revised:** 8 March 2021 / **Accepted:** 8 March 2021

ABSTRACT

Electrocatalytic hydrogen production in alkaline media is extensively adopted in industry. Unfortunately, further performance improvement is severely impeded by the retarded kinetics, which requires the fine regulation of water dissociation, hydrogen recombination, and hydroxyl desorption. Herein, we develop a multi-interface engineering strategy to make an elaborate balance for the alkaline hydrogen evolution reaction (HER) kinetics. The graphene cross-linked three-phase nickel sulfide (NiS-NiS_2-Ni_3S_4) polymorph foam (G-NNNF) was constructed through hydrothermal sulfidation of graphene wrapped nickel foam as a three-dimensional (3D) scaffold template. The G-NNNF exhibits superior catalytic activity toward HER in alkaline electrolyte, which only requires an overpotential of 68 mV to drive 10 mA·cm^{-2} and is better than most of the recently reported metal sulfides catalysts. Density functional theory (DFT) calculations verify the interfaces between nickel sulfides (NiS/NiS_2/Ni_3S_4) and cross-linked graphene can endow the electrocatalyst with preferable hydrogen adsorption as well as metallic nature. In addition, the electron transfer from Ni_3S_4/NiS_2 to NiS results in the electron accumulation on NiS and the hole accumulation on Ni_3S_4/NiS_2, respectively. The electron accumulation on NiS favors the optimization of the H* adsorption, whereas the hole accumulation on Ni_3S_4 is beneficial for the adsorption of H_2O. The work about multi-interface collaboration pushes forward the frontier of excellent polymorph catalysts design.

KEYWORDS

hydrogen evolution reaction, nickel sulfide, interface engineering, polymorph, heterointerface

1 Introduction

Electrochemical water splitting driven by renewable solar, wind and geothermal energy has been developed into a promising and environmentally friendly pathway to provide high-purity hydrogen energy [1, 2]. Electrocatalytic hydrogen production in alkaline media is extensively adopted in industry especially due to the fact that oxygen evolution reaction (OER) in alkaline media, i.e., anodic half reaction of water splitting, is extremely preferable to acid condition. Hydrogen evolution reaction (HER) in alkaline media is also a fundamental yet significant cathode process for hydrogen-related reactions, such as the hydrogenation reactions of CO_2, N_2 and various biomass. The overall reaction pathway of alkaline HER can be illustrated by equations: ($H_2O + e^- \rightarrow H^* + OH^-$ (Volmer: discharge step); $H_2O + e^- + H^* \rightarrow H_2 + OH^-$ (Heyrovsky: electrochemical desorption step) or $2H^* \rightarrow H_2 + OH^-$ (Tafel: recombination step) [3–5]. Three most possible scenarios, i.e., water dissociation, hydrogen recombination, and hydroxyl desorption, result in retarded kinetics in alkaline media [6, 7], which is approximately two/three orders of magnitude slower than that in acid condition [8]. Unfortunately, the most effective HER electrocatalysts in alkaline condition are still severely restricted to noble metals. Therefore, it is especially urgent to develop highly active non-noble HER catalysts in alkaline media.

As a component of the [NiFe] hydrogenase, nickel sulfides have been regarded as a promising catalyst candidate for electrocatalytic HER and thus have been widely investigated [9]. Nickel sulfides have multiple crystalline phases and diverse oxidation states including NiS, Ni_3S_4, Ni_3S_2, NiS_2, Ni_7S_6, Ni_9S_8, and so on, which has been proved to be kinetics-controlled depending on the relative concentration of nickel and sulfur precursors in the synthetic system [10–14]. Unfortunately, the Gibbs free energy of hydrogen adsorption (ΔG_{H^*}) of pure-phase nickel sulfide is usually far from an ideal value of $\Delta G_{H^*} = 0$ [15]. The density of states suggests a large band gap implying high resistance and hence low conductivity of nickel sulfides. As a result, pure-phase NiS, NiS_2, and Ni_3S_2 need very high

Address correspondence to Haiqing Wang, ifc_wanghq@ujn.edu.cn; Shuxian Hu, hushuxian@csrc.ac.cn; Hong Liu, hongliu@sdu.edu.cn

overpotentials of 474, 454, and 335 mV, respectively, to drive a current density of 10 mA·cm^{-2} in alkaline environment [16]. Recently, Markovic et al. suggested the active centers are relevant to the valence of transition metal cation and anions for water dissociation (Mo^{4+} > Co^{2+}), adsorption of H^*(S^{2-} > S^-) and OH^* (Co^{2+} > Mo^{4+}) adsorption (">" means "superior to") [17]. The interface engineering between different phases or components has been developed into an effective strategy to balance the alkaline HER process [3, 15, 18–20]. Under this concept, hybrids of Pt-Ni(OH)$_2$ and MoS_2-layered double hydroxides (LDH) were reported to offer distinct sites for H* (on Pt and MoS_2) and H_2O^* (on Ni(OH)$_2$ and LDH) [21, 22]. Another work reported a complex of 2D MoN-C_3N_4 that provides MoN and C_3N_4 sites to adsorb OH* and H*, respectively [23]. Taken together, the challenge for the design of high-efficiency nickel sulfide electrocatalysts for alkaline HER is to address three major issues: (i) intrinsic activity, (ii) active site amount, and (iii) charge transport, through effectively manipulating interfacial and electronic structure.

Herein, a multi-interface engineering strategy was developed to address the major issues in alkaline HER. Graphene cross-linked three-phase nickel sulfide (NiS-NiS_2-Ni_3S_4) polymorph foam (G-NNNF) was fabricated through hydrothermal sulfidation of graphene wrapped nickel foam. The G-NNNF exhibits superior catalytic activity toward HER in alkaline electrolyte. Density functional theory (DFT) calculations verify the multi-interface engineering induced interfacial synergy among nickel sulfides (NiS/NiS_2/Ni_3S_4) and graphene for improving conductivity and balancing water dissociation and hydrogen adsorption of electrocatalyst.

2 Results and discussion

2.1 Synthesis and characterization of G-NNNF

As shown in Fig. 1, graphene wrapped nickel foam (G-F) was firstly prepared by template-directed chemical vapour deposition (CVD) via precipitating the decomposed CH_4 on the surface of nickel foam. With G-F as both template and nickel source, G-NNNF was constructed through a facile *in situ* hydrothermal sulfidation process. As for the reaction pathway, we suggest that the sulfurization of the Ni template starts from the defect locations, where Ni cation reacts with HS^- anions (NH_2CSNH_2 + $3H_2O \rightarrow HS^- + 2NH_4^+ + HCO_3^-$) forming nickel sulfides.

The introduction of NH_4F is aimed to manipulate the resultant polymorph structure by tuning the relative concentration of nickel and sulfur. Specifically, as the sulfurization goes on, the concentration of nickel cation will continuously increase. When the concentration of nickel cations attains a certain level, the sizes of nickel sulfides are getting smaller as a result of more crystal nuclei appeared according to the classical Lamer model. Owing to the inherent imperfection of nickel foam, the precipitated graphene layer inevitably has numerous defects [24] contributing to the mass transfer of nickel and sulfur sources. The nickel sulfides nanoparticles grow and deposit on the surface of graphene, while the graphene layer crosslinks throughout the nickel sulfides foam. Therefore, graphene cross-linked nickel sulfide polymorph foam is fabricated together with the elaborate manipulation of the relative concentration of nickel and sulfur ions in the synthetic system. The scanning electron microscopy (SEM) images record the evolution procedure from pristine nickel foam (Fig. 2(a) and inset), G-F (Fig. 2(b) and inset), and intermediate state (Fig. 2(c) and inset) to the resultant G-NNNF (Fig. 2(d) and inset). The nickel foam has smooth polycrystalline surface (Fig. 2(a)), which will result in defects in the deposited graphene layer. The ripples and wrinkles on the surface of G-F (Fig. 2(b)) are stemming from the divergent thermal expansion coefficients of nickel and graphene, suggesting the formation of graphene layer on the surface of nickel foam [24]. The energy-dispersive X-ray (EDX) elemental mapping suggests a uniform distribution of carbon in G-F, signifying the coherent coating of three-dimensional graphene in G-F. The intermediate state (Fig. 2(c)) corresponds to the dissolution of Ni precursor and the deposition of nickel sulfide on the outside surface of G-F. The SEM image of G-NNNF (Fig. 2(d)) suggests a highly rough surface. Note that the framework diameter of G-NNNF is about 30 μm larger than that of the pristine nickel foam, implying the formation of puffed hierarchical foam structure. The magnified SEM image of G-NNNF indicates a hierarchical structure composed of numerous interconnected substructures of irregular nanoparticles and sparse nanorods. The contact angle of water droplets on G-F and G-NNNF was also measured. The side-view images (Fig. 2(e)) illustrate that G-F has a hydrophobic surface with a biggest contact angle of ~ 120°, which should be attributed to the formation of graphene layer on the surface of nickel foam in G-F. No floating water droplets are observed on the surface of G-NNNF, suggesting a hydrophilic surface. The contact angle experiment implies the possible transformation of foam surface from graphene layer to graphene cross-linked nickel sulfides in G-NNNF. The Raman spectra of G-F, and G-NNNF are

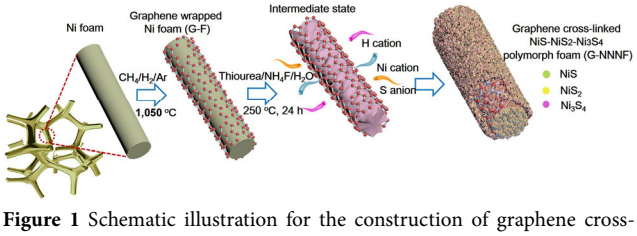

Figure 1 Schematic illustration for the construction of graphene cross-linked three-phase nickel sulfide (NiS-NiS_2-Ni_3S_4) polymorph foam (denoted as G-NNNF).

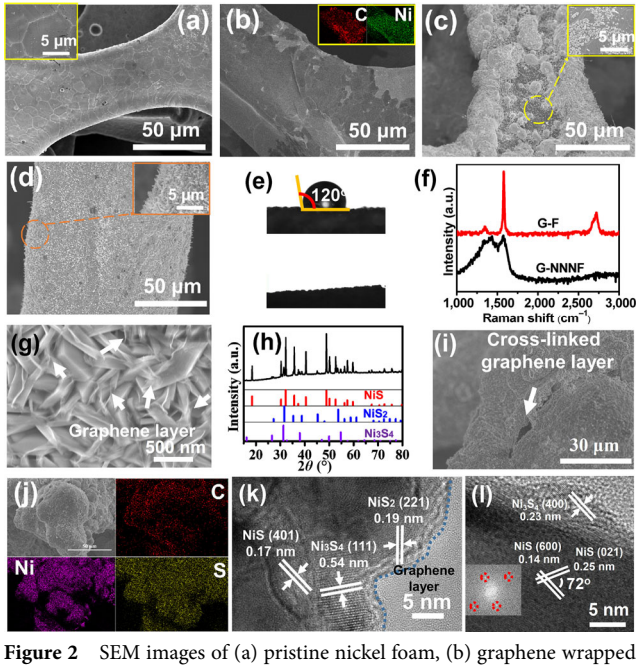

Figure 2 SEM images of (a) pristine nickel foam, (b) graphene wrapped nickel foam (G-F) with mapping image as inset, (c) intermediate state with high-magnification image of the surface as inset, and (d) the resultant G-NNNF with high-magnification image of the surface as inset. (e) Contact angle. (f) Raman pattern. (g) SEM image of G-F after acid etching. (h) XRD pattern. (i) The cross section of G-NNNF. (j) EDX mapping image. (k) and (l) HRTEM images of G-NNNF.

shown in Fig. 2(f). Three Raman peaks located at approximately 1,350, 1,580, and 2,700 cm^{-1} correspond to D, G and 2D bands, respectively. The D peak proves the presence of defects in graphene for G-F. High intensity ratio of I_D/I_G in G-NNNF implies that more defects are formed after the hydrothermal sulfidation process. The weak and broad 2D peak of G-NNNF suggests the features of few layers in the precipitated graphene, which implies its high electrical conductivity according to the reference in which the maximum conductivity is observed for graphene with about five average layers [24]. The Raman results indicate the coating of graphene on the surface of nickel foam as well as the reservation of graphene component in the resultant G-NNNF. In order to give a straightforward evidence about the cross-linking state of graphene, the G-F was etched with acid and the corresponding SEM image (Fig. 2(g)) indicates the graphene component is soft as gauzy veil. The result implies that the graphene can cross-link throughout the three-phase nickel polymorph foam. The whole graphene veil has been proved to be about six orders of magnitude higher electrical conductivity than chemically derived graphene [24, 25], which can provide robust charge transport network for the resultant G-NNNF. The X-ray diffraction (XRD) pattern of G-NNNF is shown in Fig. 2(h), which distinctly exhibits three kinds of crystalline phases, i.e., NiS (JCPDS No. 12-0041), NiS_2 (JCPDS No. 11-0099), and Ni_3S_4 (JCPDS No. 47-1739). The XRD patterns of pristine nickel foam and graphene cross-linked two-phase nickel sulfide (NiS-Ni_3S_4) foam (G-NNF) are shown in Figs. S1 and S2 in the Electronic Supplementary Material (ESM), respectively. The absence of nickel peaks in G-NNF and G-NNNF verifies the complete transformation of metallic Ni into nickel sulfide composites through the sulfurization procedure. Moreover, the SEM image of the cross section of G-NNNF (Fig. 2(i)) presents a clear opening, which reflects the presence of cross-linked graphene layer throughout G-NNNF. The EDX elemental mapping of G-NNNF (Fig. 2(j)) indicates the uniform distribution of carbon, nickel, and sulfur elements. Besides, The high-resolution transmission electron microscope (HRTEM) image of G-NNNF (Fig. 2(k)) clearly reveals the presence of interconnected NiS, NiS_2, Ni_3S_4, and graphene judging from the fact that the lattice fringe spaces of 0.17, 0.54, and 0.19 nm of the nanoparticles (~ 5–10 nm) are relevant to the (401) of NiS, (111) of Ni_3S_4 and (221) of NiS_2, respectively. While the nanorod is verified to be NiS and the nanoparticle bonded on its surface is Ni_3S_4 (Fig. 2(l)). The aforementioned results signify the realization of multi-interface engineering in the resultant G-NNNF.

The nitrogen physisorption isotherm of G-NNNF was tested and the result is shown in Fig. 3(a). The specific surface area (S_{BET}) of G-NNNF was calculated to be approximately 12 $m^2 \cdot g^{-1}$, which is significantly higher than ~ 1.0 $m^2 \cdot g^{-1}$ of pristine nickel foam. The result implies the presence of rich porosity in G-NNNF, which is expected to facilitate the mass transport of electrolyte. The surface composition and chemical states of pristine nickel foam, G-F and G-NNNF are investigated with X-ray photoelectron spectroscopy (XPS) tests. As shown in Fig. 3(b), the full XPS spectrum of pristine nickel foam indicates the presence of Ni, C and O elements. The O signal is likely attributed to the superficially partial oxidation of nickel metal. The C signal should result from the residual organic species or the contamination of CO_2 in the air. By contrast, the invisible Ni signal, the very strong C signal and the weak O signal in G-F precisely demonstrate the screening of metal signal, implying the successful coating of compact graphene carbon layer on the outer surface of nickel foam. The distinct sulfur signal only observed for G-NNNF suggests the formation of nickel sulfides after the hydrothermal sulfurization process. As shown in Fig. 3(c), the four peaks in Ni $2p_{3/2}$ spectrum arising at about 852.8, 853.8, 855.6, and 860.0 eV are well corresponding to Ni^0, Ni^{2+}, Ni^{3+}, and shakeup satellite, respectively. The pristine nickel foam suggests the signal of Ni^0 and a higher proportion of Ni^{2+} species caused by the inevitable surface oxidation of nickel as indicated by a shift to higher biding energy by about 0.5 eV [26]. The signal of Ni $2p_{3/2}$ in G-F is very weak and the nickel mainly exists in the form of Ni^0 without oxidized species, further verifying the successful and compact wrapping of graphene on the surface of nickel foam. G-NNNF demonstrates the presence of Ni^{2+} and Ni^{3+} (Fig. 3(d)) [27, 28]. Generally, the Ni 2p spectra of nickel sulfides with different crystalline phases are similar due to the fact that the Ni $2p_{3/2}$ featured nickel metal rather than sulfur atoms (Fig. S3 in the ESM) [29]. The S 2p spectrum of G-NNNF is shown in Fig. 3(e). The peaks at ~ 161.9 and ~ 162.9 eV can be attributed to S $2p_{3/2}$ and S $2p_{1/2}$ of S^{2-} in NiS/Ni_3S_4 [30]. The signals of S $2p_{3/2}$ and S $2p_{1/2}$ of NiS_2 are observed at binding energy of ~ 162.9 eV and ~ 164.0 eV, respectively. The peak at ~ 162.9 eV corresponds to the overlap of S^{2-} $2p_{1/2}$ and S_2^{2-} $2p_{3/2}$ peaks [19, 31, 32]. The peak located at approximately 168.9 eV in the S 2p region should be assigned to the superficial oxidation of nickel sulfide. Moreover, compared with G-NNF (Fig. 3(f)), the S 2p signal in G-NNNF shifts to higher binding energy by about 0.9 eV. The positive shift of S spectrum implies the presence of more positively charged S atom in G-NNNF, which is beneficial for the desorption of hydrogen atom [17]. As exhibited in Fig. S4 in the ESM, the C 1s XPS spectra of G-NNNF can be fitted with four types of carbon atoms: C–C and C=C (non-oxygenated carbon, 284.8 eV), C–O in hydroxyl and epoxide (~ 285.7 eV), C=O (carbonyl carbon, ~ 287.0 eV), and O–C=O (carboxyl carbon, ~ 288.6 eV) [33]. The XPS results suggest the co-existence of Ni^{2+}, Ni^{3+}, S^{2-}, and S^- species of different valences as well as the remained graphene component in graphene cross-linked three-phase nickel sulfide (NiS-NiS_2-Ni_3S_4) of G-NNNF, which is well consistent with the above XRD, SEM and TEM characterizations [3, 31, 34].

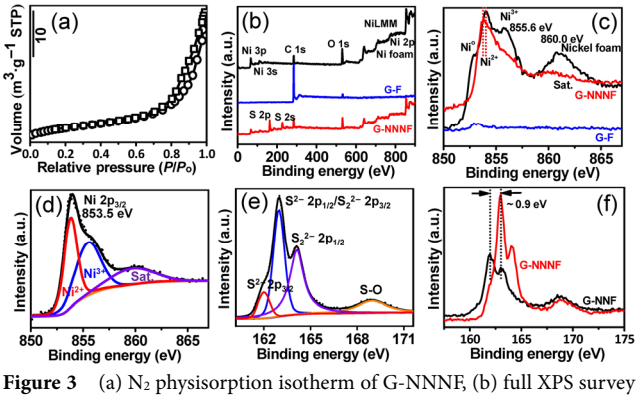

Figure 3 (a) N_2 physisorption isotherm of G-NNNF, (b) full XPS survey spectra and (c) Ni 2p peaks of nickel foam, G-F and G-NNNF. (d) Ni 2p and (e) S 2p peaks of G-NNNF. (f) S 2p peaks of G-NNF and G-NNNF.

Specifically, the HER process in alkaline electrolyte includes three consecutive state changes, i.e., the incipient state of catalyst-water, the intermediate state of H-catalyst, and the eventual state of H_2-catalyst [35]. From the perspective of structure–activity relationship, Markovic et al. [17] suggested the active centers for water dissociation (Mo^{4+} > Co^{2+}), adsorption of H^*(S^{2-} > S^-) and OH* (Co^{2+} > Mo^{4+}) adsorption are relevant to the valence of transition metal cation and anions. In this study, the positively charged nickel cations are considered to be active centers to activate the initial water-(hydroxide), while the negatively charged S center as proton acceptor forms S-H_{ads} on the surfaces of the nickel sulfide electrocatalysts. The

diverse oxidation states of Ni (+2 and +3) and S (−2 and −1) should contribute the alkaline HER kinetics. The results imply the underlying synergistic effects through multi-interfaces between different phases of nickel sulfides for alkaline HER.

2.2 HER performance evaluation of G-NNNF in alkaline electrolyte

The HER performance of the samples was investigated in an alkaline solution of H_2-saturated 1 mol·L^{-1} KOH with a standard three-electrode system. Saturated calomel electrode (SCE) and carbon rod were used as the reference electrode and the counter electrode, respectively. At the start of performance testing, the electrodes were activated and stabilized through cyclic voltammetry (CV) measurement. Note that all the data were achieved without *iR* compensation. Linear sweep voltammetry (LSV) was recorded to study the polarization ability of the electrodes. The electrocatalytic HER activities of pristine nickel foam, G-F, NNF, G-NNF, NNNF, G-NNNF, and benchmark 20 wt.% Pt/C were tested. As expected, the commercial Pt/C electrocatalyst requires a very small overpotential of about 30 mV for 10 mA·cm^{-2}. As shown in Fig. 4(a), pristine nickel foam and G-F as two references require large overpotentials of approximately 250 and 290 mV, respectively to reach 10 mA·cm^{-2}, which should be attributed to their low surface area of nickel foam and the hydrophobic surface of G-F. Interestingly, the overpotentials of NNF, G-NNF, NNNF, and G-NNNF at 10 mA·cm^{-2} decrease gradually from 188, 135, 81 to 68 mV. Compared with NNF/NNNF, the performance improvement in G-NNF/G-NNNF should be due to the positive role of graphene as a conductive cross- linking layer. The multi-interface among NiS-NiS_2-Ni_3S_4 in G-NNNF results in an obvious enhancement for HER activity compared to the two phases (NiS and Ni_3S_4) in G-NNF.

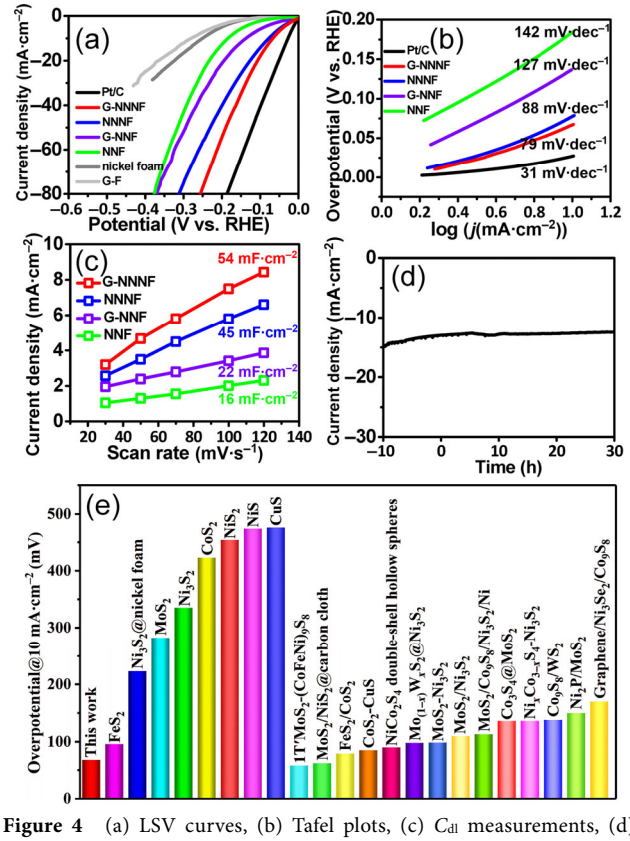

Figure 4 (a) LSV curves, (b) Tafel plots, (c) C_{dl} measurements, (d) chronoamperometric measurements (*i*–*t*) curve, and (e) comparison of the overpotentials @ 10 mA·cm^{-2} with recently reported alkaline HER electrocatalysts.

The mechanistic pathways of HER in alkaline media were firstly analyzed with Tafel plots (Fig. 4(b)). The hydrogen generation in alkaline media can be described with Volmer-Tafel or the Volmer-Heyrovsky pathway following the equations: Volmer-discharge step: $H_2O + e^- \rightarrow H^* + OH^-$; Heyrovsky-electrochemical desorption step: $H_2O + e^- + H^* \rightarrow H_2 + OH^-$ or Tafel-recombination step $2H^* \rightarrow H_2 + OH^-$. The rate-limiting step can be estimated by the values of Tafel slopes. The values of 120/40/30 mV·dec^{-1} correspond to Volmer/Heyrovsky/Tafel rate-limiting step in HER process [3]. The Tafel slopes of G-NNF and G-NNNF are 127 and 79 mV·dec^{-1}, respectively. As for G-NNF, the hydrogen evolution process is governed by the Volmer step. The Tafel slope of G-NNNF is within the range of 40–120 mV·dec^{-1}, suggesting that the Volmer step and Heyrovsky step are kinetically comparable at the process of the charge-transfer-induced water dissociation [21]. The low Tafel slope value of G-NNNF indicates a superior HER kinetics. The electrocatalytic kinetics is also evaluated by electrochemical impedance spectroscopy (EIS) analysis (Fig. S5 in the ESM). Generally, the smaller semicircles of Nyquist plots are associated with smaller charge transfer resistance (R_{ct}), thereby indicating a faster electron transfer. The lower R_{ct} of G-NNNF signifies a faster charge-transfer-induced water dissociation process for the resultant hierarchical composite foam, verifying a superior HER kinetics on the G-NNNF [36]. The essential reason of the improved HER kinetics in alkaline media should be attributed to a definite optimization in catalyst-intermediate energetics on the multi-interfaces of graphene cross-lined NiS-NiS_2-Ni_3S_4 in G-NNNF. Moreover, the electrochemical active surface area (ECSA) was roughly evaluated by double-layer capacitance (C_{dl}) test at different scanning rates in non-Faradaic region (Fig. S6 in the ESM). Figure 4(c) shows the linear correlation plots between the scan rates and current densities. The fitting line slopes of NF, G-NF, G-NNF and G-NNNF are 16, 22, 45, and 54 mF·cm^{-2}, respectively. The result implies that G-NNNF exposes more active sites for HER than its counterparts, thus leading to higher catalytic activity. The G-NNNF shows negligible catalytic degradation (~ 15% in comparison with the starting value) at about 12.5 mA·cm^{-2} for 30 h (Fig. 4(d) and Fig. S7 in the ESM), verifying good electrochemical stability of G-NNNF in alkaline HER. Moreover, it is worth noting that the overpotential of 68 mV at 10 mA·cm^{-2} delivered by G-NNNF is lower than that of most reported metal sulfides electrocatalysts (Fig. 4(e)) in 1 M KOH, such as NiS (474 mV), NiS_2 (454 mV), Ni_3S_2 (335 mV) [16], high-index faceted Ni_3S_2@nickel foam (223 mV) [37], FeS_2 (96 mV) [38], MoS_2 (282 mV) [39], CoS_2 (423 mV), CuS (476 mV) [40], $NiCo_2S_4$ double-shell hollow spheres (90 mV) [41], and comparable to some other heterointerfaces, such as defect-rich MoS_2/NiS_2@carbon cloth (62 mV) [19], MoS_2/Ni_3S_2 (110 mV) [42], FeS_2/CoS_2 (79 mV) [43], Co_9S_8/WS_2 (138 mV) [44], MoS_2-Ni_3S_2 (98/99 mV) [45, 46], Co_3S_4@MoS_2 (136 mV) [47], Graphene/Ni_3Se_2/Co_9S_8 (170 mV) [48], 1T′ MoS_2-$(CoFeNi)_9S_8$ (58 mV) [3], CoS_2-CuS (85 mV) [40], $Ni_xCo_{3-x}S_4$-Ni_3S_2 (136 mV) [49], $Mo_{(1-x)}W_xS_2$@Ni_3S_2 (98 mV) [50], Ni_2P/MoS_2 (150 mV) [39], and MoS_2/Co_9S_8/Ni_3S_2/Ni (113 mV) [36]. Thus, the graphene cross-linked NiS-NiS_2-Ni_3S_4 polymorph foam signifies the multi-interface collaboration towards the enhanced electrocatalytic activity and the robust stability, indicating the great promise of applying it as cost-effective and efficient catalyst to construct water electrolysis system in alkaline electrolytes.

2.3 The origin of HER activity in the multi-interface of G-NNNF

To further unveil the origin of the HER activity of the graphene

cross-linked NiS-NiS_2-Ni_3S_4 polymorph foam, DFT calculations were additionally performed. The adsorption energies of H* (ΔG_{H^*}) on the optimized models of the NiS, NiS@G, NiS_2@G and Ni_3S_4@G heterojunction surfaces were calculated and compared (Figs. 5(a) and 5(b)). A good HER catalyst should have a moderate ΔG_{H^*} ($|\Delta G_{H^*}| = 0$). The $|\Delta G_{H^*}|$ on Ni_3S_4@G is merely 0.111 eV, which is much smaller than that on NiS (0.253 eV), NiS@G (0.292 eV) and NiS_2@G (1.530 eV). The result signifies that the H* adsorption kinetics on the Ni_3S_4@G is preferable for the HER. Besides the moderate adsorption of Ni_3S_4@G interface, the multi-interface in G-NNNF with strong adsorption of NiS-G and weak adsorption of NiS and NiS_2@G may collaborate through the H* transfer at the interface to facilitate the HER kinetics [27]. Moreover, the density of states (DOS) of NiS@G is higher than that of pure NiS at the Fermi level (Fig. 5(c), and Fig. S8 in the ESM), the result indicates that the introduction of cross-linked graphene layer can improve the conductivity of nickel sulfide for facilitating electron transfer during electrocatalysis. In addition, the DOS patterns of NiS@G, NiS_2@G and Ni_3S_4@G reside across the Fermi level and display no band gap, implying the metallic nature of the interface between nickel sulfide and graphene. Additionally, the DOS of Ni_3S_4@G is larger than that of NiS@G and NiS_2@G at the Fermi level, demonstrating that Ni_3S_4@G has relatively high conductivity. Thus, the multi-interface in G-NNNF is suggested to manipulate the balance of H* adsorption kinetics and to improve the conductivity of the whole polymorph foam. The activity of the NiS-NiS_2 and NiS-Ni_3S_4 heterojunctions is further elucidated by calculating the difference in the electron density (Figs. 5(d) and 5(e)). The blue and pink regions refer to the electron accumulation and electron depletion area, respectively. Noticeably, the electron redistribution between NiS and NiS_2 or Ni_3S_4 occurs at the interface. The electrons transfer from Ni_3S_4 to NiS is higher than that from NiS_2 to NiS, resulting in the electron accumulation on NiS and hole accumulation on Ni_3S_4 or NiS_2. The electron accumulation on NiS favors the optimization of the H* adsorption energies and thus improves the HER activity, whereas the hole accumulation on Ni_3S_4 is beneficial for the adsorption of H_2O and further results in a promoted HER performance. Thus, the DFT calculation result also verifies the great importance of the multi-interface of G-NNNF in balancing the HER kinetics in alkaline electrolyte through the interfacial electron redistribution.

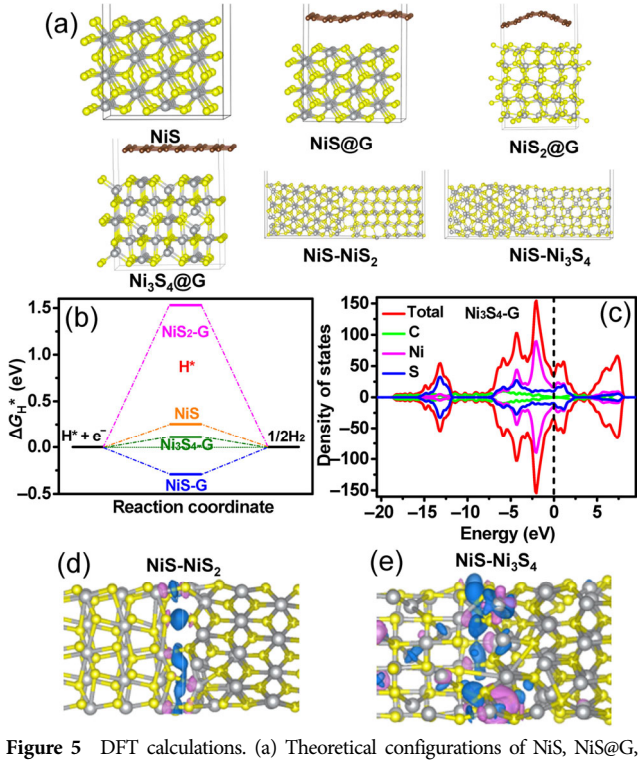

Figure 5 DFT calculations. (a) Theoretical configurations of NiS, NiS@G, NiS_2@G, Ni_3S_4@G, NiS-NiS_2 and NiS-Ni_3S_4 systems. (b) Free energy diagram for H adsorption (ΔG_{H^*}). (c) Calculated DOS curves for Ni_3S_4-graphene (Ni_3S_4-G). (d) and (e) Electron density difference plots at the NiS-NiS_2 and NiS-Ni_3S_4 interfaces.

3 Conclusions

In conclusion, a multi-interface engineering strategy was developed to make an elaborate balance for the alkaline HER kinetics. The G-NNNF has been successfully prepared through hydrothermal sulfidation of porous graphene wrapped nickel foam as a 3D scaffold template. The G-NNNF exhibits superior catalytic activity toward alkaline HER and is better than most of the recently reported metal sulfides catalysts. According to DFT calculations, the interfaces between nickel sulfides (NiS/NiS_2/Ni_3S_4) and cross-linked graphene were verified to optimize the hydrogen adsorption and simultaneously to enhance the electronic conductivity. Moreover, the electron transfer from Ni_3S_4/NiS_2 to NiS results in the electron accumulation on NiS and the hole accumulation on Ni_3S_4/NiS_2, respectively. The electron accumulation on NiS favors the optimization of the H* adsorption, whereas the hole accumulation on Ni_3S_4 is beneficial for the adsorption of H_2O. The elaborate balance between H* and H_2O adsorption induced by the multi-interface collaboration might provide an insight into designing and developing high-performance polymorph catalysts.

4 Experimental

4.1 Fabrication of graphene wrapped nickel foam (G-F)

The CVD growth of graphene on Ni foam metal substrates (2 cm × 2 cm in size and 1 mm in thickness) were used to fabricate G-F. To be specific, the nickel foams were heated to 1,050 °C and annealed for 5 min in a horizontal tube furnace under Ar (450 mL·min^{-1}) and H_2 (50 mL·min^{-1}) to eliminate the thin oxide layer on the surface of Ni foam and clean the surface for the following graphene growth. And then a small amount of CH_4 with a flow rate of 5 mL·min^{-1} (~ 1.0 vol.% in the total gas flow) was then introduced into the reaction tube at ambient pressure. After 10 min of reaction-gas mixture flow, the heating unit was moved aside and the samples were rapidly cooled to room temperature under Ar and H_2 protection.

4.2 Construction of G-NNNF

G-NNNF was prepared through a facile *in situ* hydrothermal sulfidation of G-F as both template and nickel source by elaborately manipulating reaction kinetics. Specifically, the relative concentration of nickel and sulfur ions in the synthetic system was well modulated by sulfur source and NH_4F. In a typical synthesis, 2.3 g of thiourea and 0.15 g NH_4F were dissolved into 20 mL ultrapure water and moved into a 50 mL Teflon-lined autoclave with steel shell. A piece of Ni foam@graphene (1 cm × 2 cm in size) was immersed into the above autoclave. The autoclave was sealed, heated in the oven at 250 °C for 24 h, and then was cooled down to room temperature naturally. The product was cleaned with ethanol three times and dried in vacuum at room temperature. The G-NNF was prepared with similar procedure but 0.08 g NH_4F. The corresponding G-NNN/G-NN were prepared without the process of graphene coating.

4.3 Characterizations

XRD patterns of the samples were measured on a Bruker D8 Advance X-ray diffractometer using Cu Kα radiation (λ = 1.541,8 Å). SEM images were acquired with a Hitachi SU8010 field emission gun scanning electron microscope at 5 kV. TEM graphs were observed by using a Hitachi H-7700 TEM operating at 100 kV. HRTEM, dark-field scanning transmission electron microscopy (STEM), as well as EDX element mapping tests were performed on a FEI Tecnai G2 F20 STwin microscope at 200 kV. N_2 adsorption–desorption isotherms were measured on a Micromeritics ASAP 2010 automatic adsorption instrument at 77 K. Before the measurements, calcined samples were degassed in vacuum at 150 °C for 2 h. Surface areas were calculated using the Brunauer-Emmett-Teller (BET) equation. XPS signals were collected by a Thermo Fisher ESCALAB 250Xi spectrometer applying monochromatic Al Kα X-ray sources (1,486.6 eV) at 2.0 kV and 20 mA.

4.4 Electrocatalytic measurements

The electrochemical tests were performed 1 M KOH media with a three-electrode system at an electrochemical station (Shanghai Chenhua, CHI 760E), using SCE as the reference electrode and carbon rod as the counter electrodes. All potentials were referenced to reversible hydrogen electrode (RHE) by following calculations: E (vs. RHE) = E (SCE) + 0.242 + 0.059pH. The polarization curves and Tafel plots were tested in the selected potential ranges at a scan rate of 5 mV·s^{-1}. The Nyquist plots of EIS measurements were performed with frequency from 0.1 to 100,000 Hz at an overpotential of 180 mV for HER. A chronoamperometry (i–t) technique was used to test long-term stability. The cyclic voltammetry was used to evaluate electrochemical C_{dl} at no faradic processes at different scan rates. The ECSA values were roughly calculated according to the calculation ECSA(cm^2_{ECSA}) = C_{dl}/40 μF·cm^2.

4.5 Theoretical computation methods

The crystal structures of NiS (110) and heterojunction NiS (110)-graphene, NiS_2 (010)-graphene, Ni_3S_4 (100)-graphene were constructed by 2 × 1, 2 × 1, 2 × 2, 2 × 2 supercells with a vacuum spacing of 15 Å to avoid interaction between adjacent surfaces. All the calculations were performed using DFT within the Perdew-Burke-Ernzerhof (PBE) parameterization of generalized gradient analysis (GGA), as implemented in the Vienna ab initio simulation package (VASP) code. The projector augmented wave (PAW) method was employed to describe electron–ion interactions. Brillouin zone (BZ) sampling used a grid with spacing of 3 × 3 × 1 and a plane-wave basis cut-off set at 400 eV. Spin-polarized local density approximation plus on-site Coulomb self-interaction potential (LDA + U) calculations were performed for the Hubbard correction, and an effective U (U_{eff}) value of 3.5 eV was applied in all calculations. Equilibrium geometries were obtained by the minimum energy principle until the energy and force converged to 10^{-4} eV and 0.02 eV·Å^{-1}, respectively.

The Gibbs free energy of the intermediates were calculated as

$$\Delta G_0 = \Delta E_{ad} + \Delta E_{ZPE} - T\Delta S \quad (1)$$

where ΔE_{ad} is the binding energy. ΔE_{ZPE} and ΔS, which can be obtained from the vibration energy of intermediates.

The gas-phase H_2O at 0.035 bar is used as the reference state because it is in equilibrium with liquid water at 300 K. The free energy of ($H^+ + e^-$) is calculated as the free energy of ½ H_2 (1 bar, 298 K) since the reference potential is standard hydrogen electrode, as displayed in Eq. (2). The energy of ($OH^- - e^-$) is calculated with Eq. (3)

$$(H^+ + e^-) \rightarrow ½\ H_2 \quad (2)$$

$$H_2O \rightarrow (H^+ + e^-) + (OH^- - e^-) \quad (3)$$

The reaction free energy of processes $\Delta G_{(U, pH)}$ is calculated as

$$\Delta G_{(U, pH)} = \Delta G_0 + \Delta G_{pH} + \Delta G_U \quad (4)$$

$$\Delta G_U = -eU \quad (5)$$

$$\Delta G_{pH} = -k\cdot T\cdot\ln[H^+] = k\cdot T\cdot\ln10\cdot pH \quad (6)$$

ΔG_{pH} is the correction of a pH different from 0 and ΔG_U is the correction of bias in which U is the electrode potential relative to the standard hydrogen electrode.

Acknowledgements

This work was supported by the National Key Research and Development Program of China (No. 2017YFB0405400), Shandong Provincial Natural Science Foundation (Nos. ZR2019BB025 and ZR2018ZC0842), the Project of "20 items of University" of Jinan (No. 2018GXRC031), the National Natural Science Foundation of China (Nos. 21976014, U1930402 and 22071172), and the generous computer time from TianHe2-JK Supercomputer Center.

Electronic Supplementary Material: Supplementary material (further details of XRD, XPS, EIS Nyquist plots, Non-Faradaic scan for double-layer capacitance, DOS calculations of reference samples) is available in the online version of this article at https://doi.org/10.1007/s12274-021-3445-5.

References

[1] Li, H. Y.; Chen, S. M.; Jia, X. F.; Xu, B.; Lin, H. F.; Yang, H. Z.; Song, L.; Wang, X. Amorphous nickel-cobalt complexes hybridized with 1T-phase molybdenum disulfide via hydrazine-induced phase transformation for water splitting. *Nat. Commun.* **2017**, *8*, 15377

[2] Ni, B.; He, P.; Liao, W. X.; Chen, S. M.; Gu, L.; Gong, Y.; Wang, K.; Zhuang, J.; Song, L.; Zhou, G. et al. Surface oxidation of AuNi heterodimers to achieve high activities toward hydrogen/oxygen evolution and oxygen reduction reactions. *Small* **2018**, *14*, 1703749

[3] Li, H. Y.; Chen, S. M.; Zhang, Y.; Zhang, Q. H.; Jia, X. F.; Zhang, Q.; Gu, L.; Sun, X. M.; Song, L.; Wang, X. Systematic design of superaerophobic nanotube-array electrode comprised of transition-metal sulfides for overall water splitting. *Nat. Commun.* **2018**, *9*, 2452.

[4] Liu, D. L.; Zhang, C.; Yu, Y. F.; Shi, Y. M.; Yu, Y.; Niu, Z. Q.; Zhang, B. Hydrogen evolution activity enhancement by tuning the oxygen vacancies in self-supported mesoporous spinel oxide nanowire arrays. *Nano Res.* **2018**, *11*, 603–613.

[5] Hua, W.; Sun, H. H.; Xu, F.; Wang, J. G. A review and perspective on molybdenum-based electrocatalysts for hydrogen evolution reaction. *Rare Met.* **2020**, *39*, 335–351.

[6] Cheng, T.; Wang, L.; Merinov, B. V.; Goddard III, W. A. Explanation of dramatic pH-dependence of hydrogen binding on noble metal electrode: Greatly weakened water adsorption at high pH. *J. Am. Chem. Soc.* **2018**, *140*, 7787–7790.

[7] Lu, H. Y.; Fan, W.; Huang, Y. P.; Liu, T. X. Lotus root-like porous carbon nanofiber anchored with CoP nanoparticles as all-pH hydrogen evolution electrocatalysts. *Nano Res.* **2018**, *11*, 1274–1284.

[8] Wei, J.; Zhou, M.; Long, A. C.; Xue, Y. M.; Liao, H. B.; Wei, C.; Xu, Z. J. Heterostructured electrocatalysts for hydrogen evolution reaction under alkaline conditions. *Nano-Micro Lett.* **2018**, *10*, 75.

[9] Wang, Z. Y.; Li, R. L.; Su, C. L.; Loh, K. P. Intercalated phases of transition metal dichalcogenides. *SmartMat* **2020**, *1*, e1013.

[10] Lv, J.; Cheng, Y.; Liu, W.; Quan, B.; Liang, X. H.; Ji, G. B.; Du, Y. W. Achieving better impedance matching by a sulfurization method through converting Ni into NiS/Ni_3S_4 composites. *J. Mater. Chem.*

C **2018**, *6*, 1822–1828.
[11] Barim, G.; Smock, S. R.; Antunez, P. D.; Glaser, D.; Brutchey, R. L. Phase control in the colloidal synthesis of well-defined nickel sulfide nanocrystals. *Nanoscale* **2018**, *10*, 16298–16306.
[12] Dai, C.; Li, B.; Li, J.; Zhao, B.; Wu, R. X.; Ma, H. F.; Duan, X. D. Controllable synthesis of NiS and NiS_2 nanoplates by chemical vapor deposition. *Nano Res.* **2020**, *13*, 2506–2511.
[13] Zhu, J. H.; Chen, Z.; Jia, L.; Lu, Y. Q.; Wei, X. R.; Wang, X. N.; Wu, W. D.; Han, N.; Li, Y. G.; Wu, Z. X. Solvent-free nanocasting toward universal synthesis of ordered mesoporous transition metal sulfide@N-doped carbon composites for electrochemical applications. *Nano Res.* **2019**, *12*, 2250–2258.
[14] Dong, Q. C.; Zhang, Y. Z.; Dai, Z. Y.; Wang, P.; Zhao, M.; Shao, J. J.; Huang, W.; Dong, X. C. Graphene as an intermediary for enhancing the electron transfer rate: A free-standing Ni_3S_2@graphene@Co_9S_8 electrocatalytic electrode for oxygen evolution reaction. *Nano Res.* **2018**, *11*, 1389–1398.
[15] Guo, Y. N.; Park, T.; Yi, J. W.; Henzie, J.; Kim, J.; Wang, Z. L.; Jiang, B.; Bando, Y.; Sugahara, Y.; Tang, J. et al. Nanoarchitectonics for transition-metal-sulfide-based electrocatalysts for water splitting. *Adv. Mater.* **2019**, *31*, 1807134.
[16] Jiang, N.; Tang, Q.; Sheng, M.; You, B.; Jiang, D. E.; Sun, Y. J. Nickel sulfides for electrocatalytic hydrogen evolution under alkaline conditions: A case study of crystalline NiS, NiS_2, and Ni_3S_2 nanoparticles. *Catal. Sci. Technol.* **2016**, *6*, 1077–1084.
[17] Staszak-Jirkovský, J.; Malliakas, C. D.; Lopes, P. P.; Danilovic, N.; Kota, S. S.; Chang, K. C.; Genorio, B.; Strmcnik, D.; Stamenkovic, Vojislav R.; Kanatzidis, M. G. et al. Design of active and stable Co–Mo–S_x chalcogels as pH-universal catalysts for the hydrogen evolution reaction. *Nat. Mater.* **2016**, *15*, 197–203.
[18] Centi, G. Smart catalytic materials for energy transition. *SmartMat* **2020**, *1*, e1005.
[19] Lin, J. H.; Wang, P. C.; Wang, H. H.; Li, C.; Si, X. Q.; Qi, J. L.; Cao, J.; Zhong, Z. X.; Fei, W. D.; Feng, J. C. Defect-rich heterogeneous MoS_2/NiS_2 nanosheets electrocatalysts for efficient overall water splitting. *Adv. Sci.* **2019**, *6*, 1900246.
[20] Wang, H. Q.; Xu, X. B.; Ni, B.; Li, H. Y.; Bian, W.; Wang, X. 3D self-assembly of ultrafine molybdenum carbide confined in N-doped carbon nanosheets for efficient hydrogen production. *Nanoscale* **2017**, *9*, 15895–15900.
[21] Hu, J.; Zhang, C. X.; Jiang, L.; Lin, H.; An, Y. M.; Zhou, D.; Leung, M. K. H.; Yang, S. H. Nanohybridization of MoS_2 with layered double hydroxides efficiently synergizes the hydrogen evolution in alkaline media. *Joule* **2017**, *1*, 383–393.
[22] Wang, P. T.; Zhang, X.; Zhang, J.; Wan, S.; Guo, S. J.; Lu, G.; Yao, J. L.; Huang, X. Q. Precise tuning in platinum-nickel/nickel sulfide interface nanowires for synergistic hydrogen evolution catalysis. *Nat. Commun.* **2017**, *8*, 14580.
[23] Jin, H. Y.; Liu, X.; Jiao, Y.; Vasileff, A.; Zheng, Y.; Qiao, S. Z. Constructing tunable dual active sites on two-dimensional C_3N_4@MoN hybrid for electrocatalytic hydrogen evolution. *Nano Energy* **2018**, *53*, 690–697.
[24] Chen, Z. P.; Ren, W. C.; Gao, L. B.; Liu, B. L.; Pei, S. F.; Cheng, H. M. Three-dimensional flexible and conductive interconnected graphene networks grown by chemical vapour deposition. *Nat. Mater.* **2011**, *10*, 424–428.
[25] Zhang, B.; Hou, J. G.; Wu, Y. Z.; Cao, S. Y.; Li, Z. W.; Nie, X. W.; Gao, Z. M.; Sun, L. C. Tailoring active sites in mesoporous defect-rich NC/V_o-WON heterostructure array for superior electrocatalytic hydrogen evolution. *Adv. Energy Mater.* **2019**, *9*, 1803693.
[26] Wang, H. Q.; Zhang, X. W.; Wang, J. G.; Liu, H. L.; Hu, S. L.; Zhou, W. J.; Liu, H.; Wang, X. Puffing quaternary $Fe_xCo_yNi_{1-x-y}P$ nanoarray via kinetically controlled alkaline etching for robust overall water splitting. *Sci. China Mater.* **2020**, *63*, 1054–1064.
[27] Zhang, Z. F.; Wang, H. Q.; Ma, M. J.; Liu, H. L.; Zhang, Z. C.; Zhou, W. J.; Liu, H. Integrating NiMoO wafer as a heterogeneous 'turbo' for engineering robust Ru-based electrocatalyst for overall water splitting. *Chem. Eng. J.* **2020**, 127686.
[28] Pothu, R.; Bolagam, R.; Wang, Q. H.; Ni, W.; Cai, J. F.; Peng, X. X.; Feng, Y. Z.; Ma, J. M. Nickel sulfide-based energy storage materials for high-performance electrochemical capacitors. *Rare Met.* **2021**, *40*, 353–373.
[29] Luo, P.; Zhang, H. J.; Liu, L.; Zhang, Y.; Deng, J.; Xu, C. H.; Hu, N.; Wang, Y. Targeted synthesis of unique nickel sulfide (NiS, NiS_2) microarchitectures and the applications for the enhanced water splitting system. *ACS Appl. Mater. Interfaces* **2017**, *9*, 2500–2508.
[30] Wang, H. Q.; Xu, Z. F.; Zhang, Z. F.; Hu, S. X.; Ma, M. J.; Zhang, Z. C.; Zhou, W. J.; Liu, H. Addressable surface engineering for N-doped WS_2 nanosheet arrays with abundant active sites and the optimal local electronic structure for enhanced hydrogen evolution reaction. *Nanoscale* **2020**, *12*, 22541–22550.
[31] Ni, B.; He, T.; Wang, J. O.; Zhang, S. M.; Ouyang, C.; Long, Y.; Zhuang, J.; Wang, X. The formation of $(NiFe)S_2$ pyrite mesocrystals as efficient pre-catalysts for water oxidation. *Chem. Sci.* **2018**, *9*. 2762–2767.
[32] Wu, T. X.; Zhu, X. G.; Wang, G. Z.; Zhang, Y. X.; Zhang, H. M.; Zhao, H. J. Vapor-phase hydrothermal growth of single crystalline NiS_2 nanostructure film on carbon fiber cloth for electrocatalytic oxidation of alcohols to ketones and simultaneous H_2 evolution. *Nano Res.* **2018**, *11*, 1004–1017.
[33] Kong, L.; Tang, C.; Peng, H. J.; Huang, J. Q.; Zhang, Q. Advanced energy materials for flexible batteries in energy storage: A review. *SmartMat* **2020**, *1*, e1007.
[34] Li, Q.; Wang, D. W.; Han, C.; Ma, X.; Lu, Q. Q.; Xing, Z. C.; Yang, X. R. Construction of amorphous interface in an interwoven NiS/NiS_2 structure for enhanced overall water splitting. *J. Mater. Chem. A* **2018**, *6*, 8233–8237.
[35] Fang, Z. W.; Peng, L. L.; Qian, Y. M.; Zhang, X.; Xie, Y. J.; Cha, J. J.; Yu, G. H. Dual tuning of Ni-Co-A (A = P, Se, O) nanosheets by anion substitution and holey engineering for efficient hydrogen evolution. *J. Am. Chem. Soc.* **2018**, *140*, 5241–5247.
[36] Yang, Y.; Yao, H. Q.; Yu, Z. H.; Islam, S. M.; He, H. Y.; Yuan, M. W.; Yue, Y. H.; Xu, K.; Hao, W. C.; Sun, G. B. et al. Hierarchical nanoassembly of MoS_2/Co_9S_8/Ni_3S_2/Ni as a highly efficient electrocatalyst for overall water splitting in a wide pH range. *J. Am. Chem. Soc.* **2019**, *141*, 10417–10430.
[37] Feng, L. L.; Yu, G. T.; Wu, Y. Y.; Li, G. D.; Li, H.; Sun, Y. H.; Asefa, T.; Chen, W.; Zou, X. X. High-index faceted Ni_3S_2 nanosheet arrays as highly active and ultrastable electrocatalysts for water splitting. *J. Am. Chem. Soc.* **2015**, *137*, 14023–14026.
[38] Miao, R.; Dutta, B.; Sahoo, S.; He, J. K.; Zhong, W.; Cetegen, S. A.; Jiang, T.; Alpay, S. P.; Suib, S. L. Mesoporous iron sulfide for highly efficient electrocatalytic hydrogen evolution. *J. Am. Chem. Soc.* **2017**, *139*, 13604–13607.
[39] Kim, M.; Anjum, M. A. R.; Lee, M.; Lee, B. J.; Lee, J. S. Activating MoS_2 basal plane with Ni_2P nanoparticles for Pt-like hydrogen evolution reaction in acidic media. *Adv. Funct. Mater.* **2019**, *29*, 1809151.
[40] Li, M. C.; Qian, Y. T.; Du, J. M.; Wu, H. R.; Zhang, L. Y.; Li, G.; Li, K. D.; Wang, W. M.; Kang, D. J. CuS nanosheets decorated with CoS_2 nanoparticles as an efficient electrocatalyst for enhanced hydrogen evolution at all pH values. *ACS Sustainable Chem. Eng.* **2019**, *7*, 14016–14022.
[41] Jiang, Y. Q.; Qian, X.; Zhu, C. L.; Liu, H. Y.; Hou, L. X. Nickel cobalt sulfide double-shelled hollow nanospheres as superior bifunctional electrocatalysts for photovoltaics and alkaline hydrogen evolution. *ACS Appl. Mater. Interfaces* **2018**, *10*, 9379–9389.
[42] Zhang, J.; Wang, T.; Pohl, D.; Rellinghaus, B.; Dong, R. H.; Liu, S. H.; Zhuang, X. D.; Feng, X. L. Interface engineering of MoS_2/Ni_3S_2 heterostructures for highly enhanced electrochemical overall-water-splitting activity. *Angew. Chem., Int. Ed.* **2016**, *55*, 6702–6707.
[43] Li, Y. X.; Yin, J.; An, L.; Lu, M.; Sun, K.; Zhao, Y. Q.; Gao, D. Q.; Cheng, F. Y.; Xi, P. X. FeS_2/CoS_2 interface nanosheets as efficient bifunctional electrocatalyst for overall water splitting. *Small* **2018**, *14*, 1801070.
[44] Peng, S. J.; Li, L. L.; Zhang, J.; Tan, T. L.; Zhang, T. R.; Ji, D. X.; Han, X. P.; Cheng, F. Y.; Ramakrishna, S. Engineering Co_9S_8/WS_2 array films as bifunctional electrocatalysts for efficient water splitting. *J. Mater. Chem. A* **2017**, *5*, 23361–23368.

[45] Yang, Y. Q.; Zhang, K.; Lin, H. L.; Li, X.; Chan, H. C.; Yang, L. C.; Gao, Q. S. MoS_2–Ni_3S_2 heteronanorods as efficient and stable bifunctional electrocatalysts for overall water splitting. *ACS Catal.* **2017**, *7*, 2357–2366.

[46] Gu, X. D.; Zheng, S. J.; Huang, X. B.; Yuan, H. F.; Li, J. P.; Kundu, M.; Wang, X. G. Hybrid Ni_3S_2–MoS_2 nanowire arrays as a pH-universal catalyst for accelerating the hydrogen evolution reaction. *Chem. Commun.* **2020**, *56*, 2471–2474.

[47] Guo, Y. N.; Tang, J.; Wang, Z. L.; Kang, Y. M.; Bando, Y.; Yamauchi, Y. Elaborately assembled core-shell structured metal sulfides as a bifunctional catalyst for highly efficient electrochemical overall water splitting. *Nano Energy* **2018**, *47*, 494–502.

[48] Hou, Y.; Qiu, M.; Nam, G.; Kim, M. G.; Zhang, T.; Liu, K. J.; Zhuang, X. D.; Cho, J.; Yuan, C.; Feng, X. L. Integrated hierarchical cobalt sulfide/nickel selenide hybrid nanosheets as an efficient three-dimensional electrode for electrochemical and photoelectrochemical water splitting. *Nano Lett.* **2017**, *17*, 4202–4209.

[49] Wu, Y. Y.; Liu, Y. P.; Li, G. D.; Zou, X.; Lian, X. R.; Wang, D. J.; Sun, L.; Asefa, T.; Zou, X. X. Efficient electrocatalysis of overall water splitting by ultrasmall $Ni_xCo_{3-x}S_4$ coupled Ni_3S_2 nanosheet arrays. *Nano Energy* **2017**, *35*, 161–170.

[50] Zheng, M. Y.; Du, J.; Hou, B. P.; Xu, C. L. Few-layered $Mo_{(1-x)}W_xS_2$ hollow nanospheres on Ni_3S_2 nanorod heterostructure as robust electrocatalysts for overall water splitting. *ACS Appl. Mater. Interfaces* **2017**, *9*, 26066–26076.